Program Digest, 2019 IEEE International Ultrasonics Symposium (IUS)
Glasgow, Scotland, October 6-9, 2019

# Phase-Insensitive Ultrasound Tomography of the Attenuation of Breast Phantoms

Christian Baker*†, Daniel Sarno†, Robert Eckersley*, Mark Hodnett† and Bajram Zeqiri†
* Biomedical Engineering Department, Division of Imaging Sciences, King's College London, London SE1 7EH, U.K
† Ultrasound and Underwater Acoustics Group, National Physical Laboratory, Teddington, Middlesex TW11 0LW, U.K
Email: christian.baker@npl.co.uk

***Abstract*—This paper describes imaging of breast phantoms using a prototype phase-insensitive ultrasound computed tomography (piUCT) system. The piUCT technique generates quantitative maps of acoustic attenuation with potential application to the detection of breast cancer. The effectiveness of the piUCT technique has been previously demonstrated in the laboratory through imaging of small, cylindrical, polyurethane phantoms. This paper presents images generated by the new system, which was designed to image breasts and breast phantoms up to 200 mm in diameter at 3.2 MHz. piUCT images are compared with XCT images and laboratory measurements of the attenuation of the constituent materials of the phantom.**

***Index Terms*—Computed tomography, Medical diagnostic imaging, Ultrasonic imaging**

## I. Introduction

Ultrasound computed tomography (UCT) has been suggested as a potential adjunct and perhaps eventual replacement to X-ray mammography due to its non-ionising, low cost and non-invasive nature [1]. The UCT technique was first described in 1974 [2], and in 1977 it was first reported that the speed of sound and acoustic attenuation of excised malignant tumour tissue was significantly different to excised healthy tissue, suggesting that quantitative imaging of the material properties of the breast could be a highly useful diagnostic tool. In recent years, the generation of accurate and high resolution quantitative maps of the sound speed of breast tissue has been achieved using UCT [3]. These systems employ arrays of phase-sensitive detectors that surround the breast and generate images using computationally-intensive reconstruction techniques such as full wave imaging (FWI). Reconstruction of high quality attenuation images, however, has proved difficult - many more iterations are required than for sound-speed imaging and the resulting images are prone to artefacts and sensitive to noise.

It has been long established that two phenomena relating to the size of the active area of a phase-sensitive detector can cause errors in the measurement of attenuation: larger transducers are more directional and suffer from phase cancellation. These phenomena are manifested strongly in attenuation measurement of breasts because the acoustic field is heavily aberrated by the highly heterogeneous properties of the tissue, resulting in ultrasound arriving at the transducer at oblique angles and with a highly structured wavefront. It was suggested early on in the development of UCT that the application of omnidirectional, phase-insensitive detectors could improve attenuation imaging.

In a previous paper, we demonstrated that a novel phase-insensitive pyroelectric sensor was capable of generating quantitative, near artefact-free images of the acoustic attenuation of cylindrical phantoms without employing computational intensive full-wave inversion [4]. This paper presents the first results generated by a new phase-insensitive UCT (piUCT) system designed to image anatomically sized breast phantoms.

## II. Materials and Methods

### A. piUCT System

The piUCT system was designed to generate 2 dimensional cross-sectional quantitative images of the acoustic attenuation of breast phantoms. The system consists of: a rotating scanning head positioned in the centre of a 120 l water tank; a chassis housing the motion stages, into which the tank is mounted; a patient couch with a breast aperture positioned directly over the water tank and scanning head; and a cabinet containing control, drive and acquisition electronics.

The scanning head consists of a 14 element linear array of ultrasound transducers positioned opposite a single element pyroelectric sensor that covers the entire width of the scan area. The breast phantom is placed in a water bath between the transducer array and sensor and scanned in a through-transmission, parallel beam configuration. A schematic diagram of the scanning head is presented in figure 1, and a photograph is shown in figure 2. During a scan, the scanning head rotates around the phantom taking projections of the acoustic insertion loss at 61 discrete angles between $0°$ and $180°$. Each projection is generated by translating the transducer array across the scan plane to 11 discrete positions each separated by $1.375\,\mathrm{mm}$ and taking a pyroelectric measurement of the insertion loss from each transducer at each position. A scan is therefore made up of 9,394 pyroelectric measurements.

The transducer array elements are $10\,\mathrm{mm}$ crystal diameter, $13.75\,\mathrm{mm}$ outer diameter plane-pistons with a centre frequency of $3.2\,\mathrm{MHz}$. This frequency was chosen to provide increased contrast in the resulting attenuation images and extend the depth over which the ultrasound beams were collimated. $3.2\,\mathrm{MHz}$ in particular was chosen due to the available piezoelectric crystals and a compromise between increased

This work was supported by the United Kingdom National Measurement System and Innovate UK.

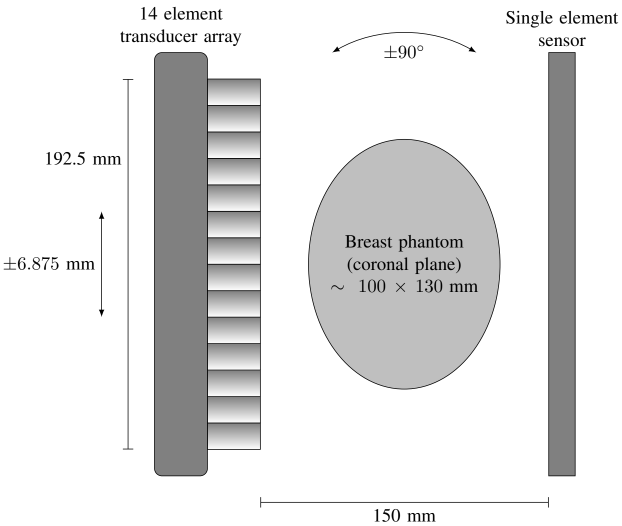


Fig. 1: Top-down schematic of the piUCT scanning head, with arrows demonstrating that the scanhead rotates around the breast and the transducer array scans laterally within the scan head.

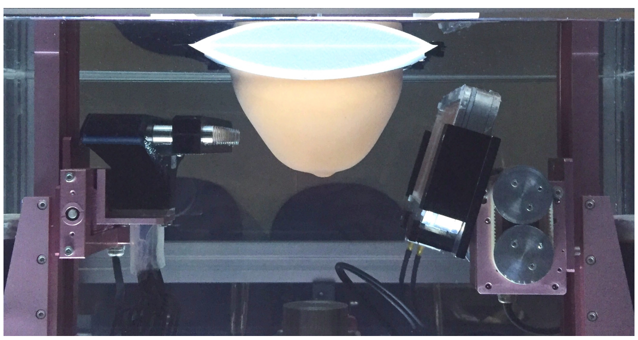

Fig. 2: A photograph of the piUCT scanning head, showing the ultrasound transducer array (left) and pyroelectric sensor (right) either side of a CIRS breast phantom.

contrast and pyroelectric signal amplitude. The array size was chosen so that a $200\,\mathrm{mm}$ area could be scanned.

The phase-insensitive sensor exploits the pyroelectric response of a thin membrane of polyvinylidene fluoride (PVDF). The PVDF membrane is laminated to a polyurethane backing material which is heated due to absorption of incident ultrasound, inducing a pyroelectric response in the PVDF proportional to the incident acoustic power. Details of the design and operation of the particular sensor employed in the piUCT system and the processing methods used to extract signal amplitudes can be found in [5]. The pyroelectric sensor responds to both the switch-on and switch-off of the source of incident ultrasound, resulting in a pyroelectric pulse with an amplitude dependent on the time between the switch-on and switch-off as described in [5]. Long acoustic signals are required compared to traditional ultrasound imaging in order to maximise the pyroelectric amplitude - typically between $1\,\mathrm{ms}$ and $6\,\mathrm{ms}$.

TABLE I: Attenuation of the constituent materials of the phantom.

| Material | Attenuation at 3.2 MHz |
|---|---|
| “Bulk” | $0.7 \pm 0.1\,\mathrm{dB\,cm^{-1}}$ |
| “Skin” | $1.0 \pm 0.1\,\mathrm{dB\,cm^{-1}}$ |

### B. Phantom Imaging

The piUCT system was used to image a CIRS (Norfolk, VA, USA) Multi-Modality Breast Biopsy and Sonographic Trainer phantom (model 073). The phantom consisted of a ‘bulk’ material surrounded by a layer of ‘skin’ material. The acoustic attenuations of the constituent materials of the phantom were known from previous measurements described in [6] and are shown in Table I. The phantom was imaged in a coronal plane $33.5\,\mathrm{mm}$ from the nipple. This plane was chosen to provide a primarily homogeneous attenuation distribution so that the spatial variation of a the resulting attenuation map could be assessed. The plane contained two small inclusions which were identified from X-ray computed tomography (XCT) images of the phantom to be small air pockets. This allowed assessment of the morphological accuracy and resolution of the piUCT technique through analysis of size and position of the air pockets.

Two images of the phantom were generated in the same plane, but with the phantom rotated by $180°$ between scans, and translated to a different position within the water tank. This allowed any systematic effects to be assessed: any features common to both images could be attributed to the system and not the phantom. The scanner was filled with room temperature deionised water for the measurements. The system was configured to generate $2\,\mathrm{ms}$ bursts of ultrasound, the start of each burst being separated by $6\,\mathrm{ms}$. The Mechanical Index of the field generated was known from previous measurements to be approximately 0.5, and the attenuated spatial-peak temporal average intensity approximately $670\,\mathrm{mW\,cm^{-2}}$. The system was powered on for one hour prior to the measurements, and the sensor and transducers were soaked during this time to remove any air adhered to their faces. Prior to the start of each scan, a water reference projection was acquired without the phantom in place. The phantom was then placed in the scanner and the vertical position of the scanning head was set. The phantom and scanning head were positioned as shown in Figure 1. The scans were completed as described in section II-A. For each projection, insertion loss was calculated in decibels as:

$$\alpha(x) = 10 \log_{10} \frac{V_w(x)}{V_p(x)}. \tag{1}$$

where $V_p(x)$ are the pyroelectric voltages measured at each transducer position $x$ through the phantom at a particular projection angle, and $V_w(x)$ are the pyroelectric voltages of the reference projection. Each set of projections was reconstructed into an attenuation image in units of decibel per centimetre using the simultaneous algebraic reconstruction

TABLE II: Mean attenuation in piUCT image ROIs.

| Scan | Attenuation at 3.2 MHz |
|---|---|
| 1 | $0.9 \pm 0.2\,\mathrm{dB\,cm^{-1}}$ |
| 2 | $0.9 \pm 0.1\,\mathrm{dB\,cm^{-1}}$ |

TABLE III: Air pocket parameters.

| Parameter | Scan 1 | Scan 2 | XCT |
|---|---|---|---|
| Pocket 1 $D$ | $5.6\,\mathrm{mm}$ | $5.6\,\mathrm{mm}$ | $\sim 1.5\,\mathrm{mm}$ |
| Pocket 2 $D$ | $3.5\,\mathrm{mm}$ | $4.1\,\mathrm{mm}$ | $\sim 2\,\mathrm{mm}$ |
| Pocket separation | $46\,\mathrm{mm}$ | $46\,\mathrm{mm}$ | $46\,\mathrm{mm}$ |

technique (SART) algorithm provided by the Scikit-Image Python software library (one iteration, $0\,\mathrm{dB\,cm^{-1}}$ minimum attenuation). Ring artefacts were removed using a bespoke correction algorithm described in [6].

### C. Image Analysis

The mean and standard deviation of the pixel values in the resulting images were assessed in a $25\,\mathrm{mm} \times 25\,\mathrm{mm}$ region of interest (ROI). The ROI was positioned at the centre of mass of the images, and contained only pixels representing the bulk material. The resulting values were compared to the known true attenuation of the material.

The air pockets were segmented from the images by applying a threshold with a value two standard deviations above the mean pixel value in the bulk material ROI. The apparent diameter $D$ of the air pockets was measured by calculating the equivalent diameter of the pixels representing each air pocket:

$$D = 2\sqrt{\frac{\Delta x^2 N}{\pi}} \tag{2}$$

where $\Delta x$ is the pixel size ($1.375\,\mathrm{mm}$) and $N$ is the number of segmented pixels representing the air pocket. The apparent distance between the two air pockets was also measured. The sizes and relative locations of the air pockets were then compared to the diameters and positions of the pockets as apparent in the XCT datasets.

## III. Results

Attenuation images reconstructed from the two sets of piUCT scan data are shown in Figure 3. The XCT image in the same plane is also shown. The region of interest within which pixel values were assessed is shown. Although the two piUCT images were generated with the phantom in different orientations, the images have been oriented so that they can be directly compared. The horizontal and vertical axes of the plots indicate position relative to the centre of mass of the images.

The means and standard deviations of the pixel values within the ROIs are shown in Table II. The attenuations in the piUCT images agree to the known attenuation of the backing material shown in Table I to within $10\,\%$. The standard deviation of the attenuation in the ROIs is up to $22\,\%$ of the mean value. This inhomogeneity is also apparent in the images in Figure 3.

The apparent diameters of the air pockets in the piUCT images are shown in Table III along with the apparent diameters in the XCT image. The pockets appear larger in the piUCT images than the XCT image. The smallest air pocket has a diameter of $1.5\,\mathrm{mm}$ in the XCT image, but appears in the piUCT images with a diameter of nearly $6\,\mathrm{mm}$, giving an indication of the point spread function of the system. The separation between the air pockets in the three images is also shown in Table III.

## IV. Discussion

The structure of the two piUCT images generated with the phantom at different orientations and positions was qualitatively very similar. However, the shape of the lower air pocket is visibly different between the two images. This is due to the spatially varying point spread function of the system, which can be derived from the shape of the ultrasound beam and analysis of the image reconstruction process. The larger appearance of the air pockets in the piUCT images compared to the XCT data gives an indication of the size of the point spread function, suggesting a spatial resolution of between $4\,\mathrm{mm}$ and $6\,\mathrm{mm}$.

The separation between the air pockets is consistent across both piUCT images and matches with the separation seen in the XCT image. This demonstrates that the morphological information in the piUCT images is accurate, repeatable and independent of the position of the phantom within the scanner.

Both piUCT images feature a low-attenuation ring between the skin and bulk materials of the phantom that is not present on the XCT image. This ring is thought to be present because the sound-speed of the skin material is lower than both that of the bulk material and the surrounding water, causing refraction that directs sound arriving at high angles of incidence away from the phantom, reducing its path through the attenuating material and therefore causing an underestimate of the attenuation. The pixel values of the bulk material outside of this dark artefact in the piUCT images are also slightly higher than the known true values, indicating that for some paths refraction causes more attenuation than would be expected from a phantom with a homogeneous sound speed distribution.

The mean attenuation values in the piUCT image ROIs are $10\,\%$ lower than the known attenuation of the bulk material. It is thought that this is due to the fact that the attenuation in the piUCT images is calculate relative to a water path measurement using a single-frequency assumption. In practice, non-linear propagation that occurs during the water path reference measurements will increase the amount of loss occurring due to absorption in the water than would be expected from a single-frequency measurement. During a scan, the presence of the phantom reduces the amplitude of the acoustic signal and therefore the generation of harmonics due to non-linear propagation and therefore a lower attenuation is measured relative to water than would be expected.

The standard deviation of the attenuation values within the piUCT image ROIs is higher than would be expected from qualitative examination of the homogeneity of the XCT image in the same region. This spatial variation is visible as patches of high and low attenuation in the piUCT images. Information provided by the phantom manufacture informed that the bulk material was embedded with a fibrous material that is likely scattering to ultrasound and therefore contributes to the spatial variation seen. It is also likely that other inclusions present in the phantom in planes above and below the one imaged may be interfering with the measurements due to the finite ultrasound beam width.

## V. Conclusion

The piUCT system was able to generate quantitative images of the attenuation of a breast phantom. The system underestimated the attenuation of the bulk material of the phantom by $10\,\%$ due to the effects of non-linear propagation. The structure of the images agreed well with that of an XCT image generated in the same plane of the phantom, although a refraction artefact was present due to the particular sound-speeds of the constituent materials of the phantom. The system appeared to have a spatial resolution of approximately $4\,\mathrm{mm}$.

## References

[1] C. K. Glide-Hurst, A. D. A. Maidment, and C. G. Orton, "Ultrasonography is soon likely to become a viable alternative to x-ray mammography for breast cancer screening," *Med. Phys.*, vol. 37, no. 9, pp. 4526–4529, Aug 2010.

[2] J. F. Greenleaf, S. A. Johnson, S. L. Lee, G. T. Hermant, and E. H. Woo, "Algebraic reconstruction of spatial distributions of acoustic absorption within tissue from their two-dimensional acoustic projections," in *Acoustical Holography*. Springer US, 1974, pp. 591–603.

[3] H. Gemmeke, T. Hopp, M. Zapf, C. Kaiser, and N. V. Ruiter, "3d ultrasound computer tomography: Hardware setup, reconstruction methods and first clinical results," *Nucl. Instrum. Methods Phys. Res.*, vol. 873, pp. 59–65, Nov 2017.

[4] B. Zeqiri, C. Baker, G. Alosa, P. N. T. Wells, and H.-D. Liang, "Quantitative ultrasonic computed tomography using phase-insensitive pyroelectric detectors." *Phys. Med. Biol.*, vol. 58, no. 15, pp. 5237–68, 2013. [Online]. Available: http://www.ncbi.nlm.nih.gov/pubmed/23852003

[5] C. Baker, D. Sarno, R. J. Eckersley, and B. Zeqiri, "Pulse pileup correction of signals from a pyroelectric sensor for phase-insensitive ultrasound computed tomography," *IEEE Trans. Instrum. Meas.*, pp. 1–12, 2018.

[6] ——, "Ring artefact correction for phase-insensitive ultrasound computed tomography," *IEEE Trans. Ultrason., Ferroelectr., Freq. Control*, in press, 2019.

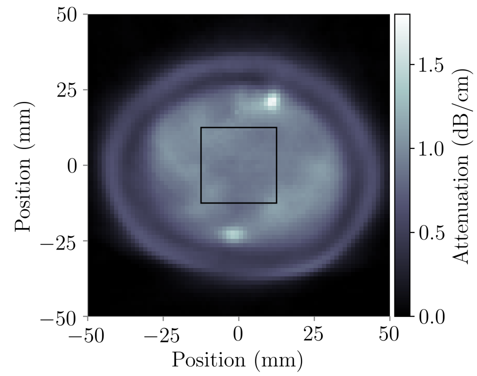


(a) Scan 1

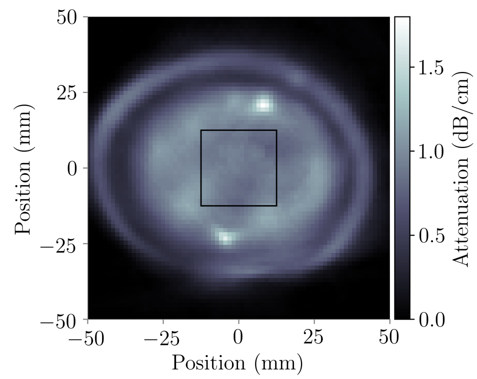


(b) Scan 2

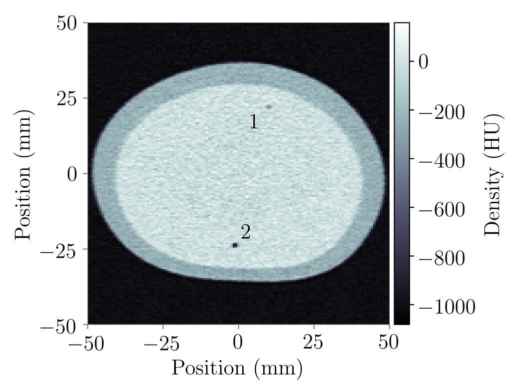


(c) XCT

Fig. 3: piUCT images and corresponding XCT image of the phantom. The images in (a) and (b) were acquired with the phantom rotated by 180° relative to one another, and translated to different positions within the water tank. The regions of interest in (a) and (b) within which pixel values were assessed are shown. The two air pockets are labelled '1' and '2' in the XCT image in (c).